Published in final edited form as:
Clin Cancer Res. 2013 May 1; 19(9): 2518–2527. doi:10.1158/1078-0432.CCR-12-2738.

Serial diffusion MRI to monitor and model treatment response of the targeted nanotherapy CRLX101

Thomas S.C. Ng[1], **David Wert**[2], **Hargun Sohi**[1], **Daniel Procissi**[1], **David Colcher**[3], **Andrew A. Raubitschek**[3], and **Russell E. Jacobs**[1]

[1]Biological Imaging Center, Beckman Institute, California Institute of Technology, Pasadena, California, USA.

[2]Department of Pathology and Microbiology, University of Nebraska Medical Center, Omaha, Nebraska, USA.

[3]Department of Cancer Immunotherapeutics & Tumor Immunology, Beckman Research Institute at City of Hope, Duarte, California, USA.

Abstract

Purpose—Targeted nanotherapies are being developed to improve tumor drug delivery and enhance therapeutic response. Techniques that can predict response will facilitate clinical translation and may help define optimal treatment strategies. We evaluated the efficacy of diffusion-weighted magnetic resonance imaging to monitor early response to CRLX101 nanotherapy (formerly IT-101), and explored its potential as a therapeutic response predictor using a mechanistic model of tumor cell-proliferation.

Experimental Design—Diffusion MRI was serially performed following CRLX101 administration in a mouse lymphoma model. Apparent diffusion coefficients (ADC) extracted from the data were used as treatment response biomarkers. Animals treated with irinotecan (CPT-11) and saline were imaged for comparison. ADC data were also input into a mathematical model of tumor growth. Histological analysis using cleaved-caspase 3, TUNEL, Ki-67 and H&E were conducted on tumor samples for correlation with imaging results.

Results—CRLX101 treated tumors at day 2, 4, 7 post-treatment exhibited changes in mean ADC=16 ± 9%, 24 ± 10% 49 ± 17% and size (TV)=−5 ± 3%, −30 ± 4% and −45 ± 13% respectively. Both parameters were statistically greater than controls ($p(ADC) \leq 0.02$, and $p(TV) \leq 0.01$ at day 4 and 7), and noticeably greater than CPT-11 treated tumors (ADC=5 ± 5%, 14 ± 7% and 18 ± 6%, TV=−15 ± 5%, −22 ± 13% and −26 ± 8%). Model-derived parameters for cell-proliferation obtained using ADC data distinguished CRLX101 treated tumors from controls ($p = 0.02$).

Conclusions—Temporal changes in ADC specified early CRLX101 treatment response and could be used to model image-derived cell-proliferation rates following treatment. Comparisons of targeted and non-targeted treatments highlight the utility of non-invasive imaging and modeling to evaluate, monitor and predict responses to targeted nanotherapeutics.

Keywords

MRI; lymphoma; nanoparticles; CRLX101; modeling

Corresponding and first author: Thomas S.C. Ng, 1200 E. California Blvd., MC 114-96, Pasadena, CA 91125, USA, Tel: 626-395-5833, Fax: 206-339-6296, flomato@cal.berkeley.edu.

Conflicts of interest
No authors have conflicts of interest to report.

Introduction

Targeted cancer nanotherapies are increasingly being explored as alternatives to conventional therapeutics. They have the potential to increase treatment efficacy and reduce treatment-related toxicity (TRT) through improved tumor drug delivery (1). Compared to conventional therapies, nanoscale therapeutics show increased plasma half-life and can localize to the tumor mass via targeting mechanisms such as enhanced permeability and retention (EPR) (2, 3). Recently, the EPR effect has been coupled with surface functionalization of particles (4) to improve retention in the tumor and target specific tumor cell subsets. Moreover, evidence exists that nanotherapies can also escape multidrug resistance pathways (3).

Nanotherapies may prove to be useful for the treatment of malignant lymphoma. Despite great advances in lymphoma management, over half of the patient population diagnosed with aggressive non-Hodgkin's lymphoma, 30–40% with advanced Hodgkin's lymphoma, and many with indolent lymphoma still develop resistance or relapse of the disease (5–7). Several strategies, including multi-drug chemotherapy, immunotherapy and radiation-based therapies, are currently being explored as salvage regimens (6, 7). Important considerations during the treatment selection process include the need to minimize TRT as well as the need to avoid cross-resistance from first-line regimens (6, 8). Thus, the use of targeted nanotherapies offers an interesting therapeutic alternative.

The nanoparticle CRLX101 (formerly IT-101, Cerulean Pharma Inc.) is a conjugate of a β-cyclodextrin-based polymer and 20(S)-campthothecin (CPT). CPT is a topoisomerase I inhibitor with a broad activity spectrum (9). CRLX101 increases the solubility of CPT, keeps CPT in its active lactone form, improves CPT tumor localization and minimizes CPT-associated TRT (10, 11). Preclinical *in vivo* studies of CRLX101 demonstrated its efficacy in a broad range of solid tumors (6, 12), including subcutaneous and disseminated xenograft lymphoma models (6). CRLX101 is currently in Phase I and Phase II trials for a variety of solid tumors (13).

A major challenge for clinical translation of cancer nanotherapies is the effective evaluation of treatment response. Imaging technologies have been used to monitor responses to conventional therapy (14). Typical methods rely on changes in tumor size (15, 16). Morphological imaging using computerized tomography (CT), ultrasound and anatomical magnetic resonance imaging (MRI) can assess changes in the appearance or growth of tumor masses. However, such changes often occur at least several weeks after treatment, which may delay useful modifications of the treatment course. A functional imaging technique, diffusion MRI (17), is being investigated to evaluate therapeutic responses in animal models (18, 19) and human clinical studies (20, 21). A quantitative metric derived from these studies, the apparent diffusion coefficient (ADC), has been shown to be sensitive to tumor therapy response. Although the diffusion of water within tumors is mediated by many complex processes, ADC has been demonstrated to be related to tumor cellularity and extracellular volume (22). Increased ADC values over the course of a treatment time course are correlated with tumor treatment response to small molecule chemotherapy (18, 19), adoptive immunotherapy (23) and photodynamic therapy (24).

Mathematical models of cancer growth attempt to predict tumor treatment response on an individual basis. Modeling adds an extra dimension to clinical management by enabling prospective, patient-specific adjustments of treatment regimens (25, 26). Non-invasive imaging data have been applied successfully to models of tumor growth and treatment response in brain (27, 28) and kidney (29) tumors . These studies demonstrate that

incorporation of imaging data into mathematical models of tumor growth can provide insights at the cellular scale that may elude conventional measures of tumor progression, such as the RECIST criteria (30). Furthermore, since the efficacy of nanotherapies is a complex function of the drug payload and the carrier's interaction with the tumor microenvironment (31), image-based modeling of treatment response may also provide mechanistic insights into the functioning of nanotherapies *in vivo*.

The purpose of this study is to determine the feasibility of diffusion MRI to evaluate and predict early treatment efficacy of the nanotherapy CRLX101. Using a preclinical model of Burkitt's lymphoma, we compared the diffusion MRI response of low dose CRLX101 to a high dose administration of a water-soluble CPT analog, irinotecan (CPT-11), and to controls. Further, serial diffusion MRI data were incorporated into a mathematical model of tumor cell proliferation to evaluate its ability to highlight and predict the anti-proliferative activity of CRLX101 *in vivo*.

Materials and Methods

Cell culture and human lymphoma xenograft models

Daudi cells (human Burkitt's lymphoma line) were obtained from the American Type Culture Collection. Cells were maintained in sterile culture media as previously described (32). 6 to 8 week old female athymic nu/nu mice (Charles River) were injected with 0.2 mL of 1:1: mixture of tumor cell suspension in 1% human serum albumin in HBSS (Mediatech) and Matrigel (BD Biosciences) subcutaneously into their right groin. Approximately 3×10^6 cells were injected for each mouse. Mouse care and experimental procedures were carried out in accordance with protocols approved by the Animal Care Committees at City of Hope and Caltech.

In vivo MRI studies

A Biospec (Bruker-Biospin Inc. Billerica, MA) 7T MRI scanner and a home-built birdcage coil were used for image acquisition. For all imaging sessions, animals were anesthetized using a 1.3–1.75% isoflurane/air mixture and body temperature was maintained at 35–37°C with warmed air flowing through the bore. For anatomical imaging, a rapid-acquisition with relaxation enhancement (*RARE*) MRI sequence (TR/TE = 4000/23 ms; RARE factor = 4; number of averages = 2; field-of-view (FOV) = 35.4 × 35.4 mm^2; image matrix = 128 × 128; slice thickness = 0.754 mm) was used to collect 40 contiguous images across the mouse torso, allowing tumor visualization.

Treatment monitoring began approximately 21 days post xenograft inoculation, when tumors reached a size of 300–800mm^3. Tumor sizes were determined from region of interests (ROI) drawn on anatomical MRI for each time point. On the day of treatment, mice were either injected with: a) 0.9% saline intravenously (i.v), b) 100mg/kg CPT-11 intraperitoneally (i.p) or c) 5mg/kg CRLX101 (i.v., dosages defined here reflect the CPT equivalent dose). Dosage and treatment cohorts were defined to be consistent with previous studies of CRLX101 (6, 12). Anatomical and diffusion MRI scans were acquired immediately before treatment (day 0, baseline), 2, 4 and 7 days post-treatment. A total of 19 mice were imaged for this study. CRLX101 and control groups contained 7 mice. Within those treatment groups, n = 3 were imaged on days 0, 2 and 4 and n = 4 were imaged on days 0, 2, 4 and 7. All mice in the CPT-11 group (n = 5) were imaged on days 0, 2, 4 and 7.

Diffusion MRI was acquired with a spin-echo diffusion MRI sequence (33) (TR/TE = 3000/25 ms; Δ = 15 ms, δ = 3 ms, with three *b* values = 0, 800, and 1,200 s/mm^2 acquired in 3 orthogonal directions; FOV = 35 × 25 mm^2; image matrix = 175 × 125 (zero-filled to 256

× 125; slice thickness = 0.754 mm). The number of slices acquired in each study was determined by the tumor size to ensure full coverage of the tumor mass.

ADC maps were generated using diffusion images by fitting to the Stejskal–Tanner equation (34). The S_0 images derived from this analysis were used as templates to segment the tumor region. Segmentation was done manually using MRIcro (www.mricro.com). Images were processed using MATLAB (Mathworks Inc).

Modeling tumor growth using diffusion MRI

A simplified logistic model of tumor growth, developed by Atuegwu et. al. (27), was applied to serial diffusion MRI data in order to estimate tumor cell proliferation rates and tumor cell number. Since it was not possible to spatially co-register tumor images from multiple time points on a voxel-by-voxel basis, we only considered ROIs based on the whole tumor. Briefly, the model is defined by:

$$N(t)=\frac{\theta N(t_1)}{N(t_1)+(\theta - N(t_1))e^{-kt}} \quad [1]$$

Where $N(t)$ is the number of cells per tumor voxel at time t, $N(t_1)$ is the number of cells present at $t = t_1$, the first time point in the calculation. k is the cell proliferative rate and θ the cell carrying capacity in the population, here assumed to be the maximum number of cells in the imaging voxel. If a linear relationship between ADC and cellularity is assumed, ADC can be related to cell number by:

$$\frac{ADC(t) - ADC_w}{ADC_{min} - ADC_w}=\left(\frac{N(t)}{\theta}\right) \quad [2]$$

and k and $N(t)$ derived by combining [1] and [2]:

$$\frac{ADC(t) - ADC_w}{ADC_{min} - ADC_w}=\left(\frac{ADC(t_1) - ADC_{min}}{ADC(t_1) - ADC_w}\right)e^{-kt}. \quad [3]$$

ADC_w is the ADC of free water (~3×10^{-3} mm^2/s) (35) and ADC_{min} is the minimum ADC value calculated from all voxels within a given tumor ROI at $t = t_1$.

The ability of the model to calculate tumor growth for this lymphoma model was tested by calculating $N_{calculated}$ (4) and $N_{calculated}$ (7) using day 0/2 and day 2/4 ADC data respectively. These were compared to $N_{esstimated}$ (4) and $N_{esstimated}$ (7), which were estimated from actual ADC data taken on day 4 and 7.

Cellular proliferation rates (k) were also calculated for each individual using a combination of ADC data between different time points (day 0/2, 0/4, 2/4, 4/7).

Histological assessment

A separate group of tumor-bearing animals (n = 24) were used to compare histological and non-invasive imaging results. The animals were treated identically as those in the imaging studies. At days 0, 2, 4 and 7, animals (n = 2 per time point) from each treatment group were sacrificed by transcardiac perfusion and tumors were excised. Tumors were placed in 4% paraformaldehyde overnight, dehydrated in 70% ethanol and subsequently embedded in paraffin. Paraffin blocks were sectioned at a slice thickness of 4 μm.

Paraffin sections were deparaffinized in xylene and rehydrated through a descending gradient of alcohol (100%, 95%, 80%, 2 minutes at each concentration) and then water.

Antigen retrieval was achieved with 10mM Tris, 1mM EDTA and 0.05% Tween 20 pH9.0 for 20 minutes in a steamer and then cooled for 20 minutes. Individual sections from each treatment cohort and time point were then incubated with primary antibodies to the cellular proliferation marker Ki-67 (1:200, Neomarkers, RM-9106-SO) or the apoptotic marker cleaved caspase-3 (CC3, 1:500, Invitrogen, 700182). Immunohistochemistry was performed on a DAKO Autostainer utilizing a peroxidase DAB method (Leica, Novalink RE7150-K) followed by counterstaining with hematoxylin.

Staining for apoptosis was performed using a terminal nucleotidyl transferase–mediated nick end labeling (TUNEL) assay (Roche, Insitu Cell Death Detection Kit) and visualized with a peroxidase DAB method (Leica, Novalink), followed by counterstaining with hematoxylin. Corresponding sections were also stained with H&E for overall tumor and cellular morphology.

All slides were scanned on a Ventana Coreo Slide Scanner for visualization. Three fields per tumor were analyzed using images obtained at 20x magnification. The percentage of Ki-67 staining was performed with ImmunoRatio (36). Hematoxylin, TUNEL and CC3 slides were analyzed using ImageJ. Slide images from each respective stain was first extracted using a color deconvolution (37) plugin; the density of cellular staining was then calculated.

Statistical analysis

Comparison of ADC, tumor size and cell proliferation data among the three treatment groups was accomplished at each time point using a Kruskal-Wallis test. Multiple comparison tests were performed with Bonferroni correction after a Mann-Whitney test. $N_{esstimated}(t)$ and $N_{calculated}(t)$ data were compared using Pearson's (PCC) and concordance (CCC) correlation coefficients. A p-value of 0.05 or smaller was considered to be statistically significant. All analyses were performed using R (http://www.r-project.org/).

Results

Diffusion MRI is sensitive to early CRLX101 treatment response

ADC maps of representative tumor response to the various treatment groups are shown in Fig. 1. ADC values remained constant for the control animal (top row) over the course of 7 days, with low ADC values (green) over most of the tumor volume at each time point. The CPT-11 treated animal (bottom row) showed a similar ADC pattern, with low ADC values over most of the tumor volume across all time points. On day 2 after CPT-11 administration, clusters of high ADC values (as indicated by red to orange pixels) can be seen around the edges of the tumor, suggesting CPT-11 response. By day 4 and day 7, small high ADC clusters still existed, but were approximately the same as seen on day 2. The ADC patterning remained similar between day 4 and day 7. Compared to the two other treatment cohorts, the CRLX101 treated tumor (middle row) showed an increase in the ADC value (shift to red) throughout the whole tumor bulk by day 2 post treatment. This increase continued onto day 4 and 7.

To compare the diffusion MRI response among treatment groups, the mean percentage change of ADC values from baseline were calculated (see Fig. 2). CRLX101 treated tumors clearly exhibited increasing tumor ADC values over the course of 7 days compared to baseline (16 ± 9%, 24 ± 10% and 49 ± 17% change from baseline on day 2, 4 and 7, respectively). CPT-11 treated tumors also showed a mean increase in ADC values over the week (5 ± 5%, 14 ± 7% and 18 ± 6%), while control tumors showed a slight decrease in ADC value compared to baseline (−4 ± 3%, −7 ± 3% and −9 ± 3%). Compared to the control group, the increases observed in the CRLX101 group were significant on all days (day 2: $p = 0.02$, day 4: $p < 0.01$, day 7: $p < 0.01$). This was not the case for the CPT-11

group (day 2: p = 0.4, day 4: p = 0.05, day 7: p = 0.05). ADC increases observed for the CRLX101 and CPT-11 cohorts were not significantly different.

Diffusion MRI response correlates with traditional measurements of tumor growth

Tumor volume changes as sorted by treatment cohort are shown in Fig. 3. Control tumors steadily increased in size during the week time course (25 ± 17%, 49 ± 15% and 130 ± 44% change from baseline on day 2, 4 and 7, respectively), while CRLX101 treated tumors steadily decreased in size (−5 ± 3%, −30 ± 4% and −45 ± 13%). As with the ADC values, size decrease in the CPT-11 treated group was less dramatic (−15 ± 5%, −22 ± 13% and −26 ± 8%) compared to the nanotherapy-treated group. The tumor size decreases in the CRLX101-treated group were not significantly different to control on day 2 (p = 0.08), but were significant by days 4 and 7 (both p < 0.01). In comparison, CPT-11 group tumor size changes were only significantly different to the control group on day 4 (p < 0.01).

Logistic model of tumor growth can be applied to diffusion MRI of malignant lymphoma

Tumor cell number determined by incorporating diffusion MRI data into a model of tumor growth is shown in Fig. 4. $N_{calculated}$ compared to $N_{esstimated}$ for days 4 and 7 are shown in Fig. 4A and 4B–C respectively. The PCC between $N_{calculated}$ (4) and $N_{esstimated}$ (4) is 0.92 ($p < 0.0001$). The CCC is 0.83. PCC and CCC between $N_{calculated}$ (7) and $N_{esstimated}$ (7) are 0.91 (p < 0.0001) and 0.9 using day 0/4 data and 0.86 (p < 0.0001) and 0.86 using day 2/4 data. These values show a strong relationship between the simulated and estimated data, demonstrating that the current simplified logistic model can be applied to the diffusion MRI data generated in this study.

Modeling of tumor proliferation using diffusion MRI show anti-proliferative activity of CRLX101

Model-derived mean cell-proliferation rates (in units of 1/day) measured from different time points across treatment groups are shown in Fig. 5. Corresponding boxplots are shown in Supplementary Fig. 1. CRLX101 treated animals showed negative tumor proliferation rates across all time points (−0.09 ± 0.05, −0.05 ± 0.03, −0.05 ± 0.01 and −0.11 ± 0.05 for day 0/2, 0/4, 2/4 and 4/7 respectively) and were significantly different ($p = 0.02$) to control tumors (0.03 ± 0.02, 0.02 ± 0.01, 0.02 ± 0.02 and 0.04 ± 0.04). CPT-11 animals (−0.04 ± 0.04, −0.02 ± 0.02, −0.06 ± 0.02 and 0.01 ± 0.01) showed negative proliferation rates between day 0 and day 4. These were significantly different to controls for rates calculated between day 2/4 ($p = 0.03$). Interestingly, proliferative rates in CPT-11 tumors calculated between day 4 and 7 became positive.

Histological assessment of CRX101 response

Treatment-induced changes observed by diffusion MRI were compared with histology (Fig. 6, Supplementary Fig. 2, and Supplementary Table 1). Tumor sections were stained for CC3 to monitor apoptotic activity (Fig. 6A, Supplementary Fig. 2A). Control tumors showed a low level of staining for CC3 throughout the week (13–110 positive stains/mm^2). By comparison, CRLX101 treated tumors showed a significant increase in CC3 activation (620±96 vs. 110±92 control, p < 0.01) on day 2. Levels remained significantly increased compared to time-matched control tumors on day 4 and day 7 (p < 0.01), albeit lower than day 2 CC3 levels. CPT-11 treated animals also showed significant increases in CC3 levels compared to control tumors on day 2 (p = 0.03) and 4 (p= 0.02), but were indistinguishable to time matched controls by day 7 (p = 0.6). Analysis using a TUNEL assay (Fig. 6B, Supplementary Fig. 2B) to stain for apoptotic cells by detecting 3′ DNA strand breaks (a biochemical hallmark of apoptosis) showed similar results. CRLX101 treated tumors showed an increase in apoptotic cells by day 2 of treatment (p < 0.01), which persisted on

day 4 and day 7. CPT-11 treated tumors showed an intermediate increase in apoptotic cells by day 2 post-treatment compared to CRLX101 tumors (350±42 vs. 470±57, $p < 0.01$ compared to controls), but were borderline different to controls by day 7 ($p = 0.05$). By comparison, control tumors did not show an increase in apoptotic cell staining throughout the week ($p > 0.4$).

Since the active ingredient of CRLX101 and CPT-11, camptothecin, inhibits cellular proliferation, we also stained tumors using the cellular proliferation marker Ki-67 (Fig. 6C, Supplementary Fig. 2C). Control tumors maintained high (94.5–98.2%) Ki-67 expression throughout the week. By comparison, both CRLX101 (46.8±5.2%, $p < 0.01$) and CPT-11 (51.7±8.2%, $p < 0.01$) treated tumors showed decreased Ki-67 staining by day 2 of treatment. Ki-67 expression in CRLX101 tumors remained significantly decreased compared to controls throughout the week ($p < 0.01$), while Ki-67 expression in CPT-11 treated tumors trended back towards control values and were borderline different to controls by day 7 ($p = 0.05$).

H&E-stained sections from the control group showed a dense cellular pattern that remained consistent from baseline to day 7 (Fig. 6D, Supplementary Fig. 2D). By comparison, CRLX101 tumors showed a gradual decrease in cellular density over 7 days (Day 0: $1.2 \times 10^4 \pm 170$ cells/mm^2, Day 7: $5.3 \times 10^3 \pm 300$, $p < 0.01$). An increase in the number of amorphous cells can be observed in day 4 and day 7 tumors. CPT-11 tumor sections show a decrease in cellular density on day 2–4 (Day 0: $1.1 \times 10^4 \pm 830$ cells/mm^2, Day 4: $5.3 \times 10^3 \pm 440$, $p < 0.01$). By day 7, the cellular patterns have trended back towards baseline ($9.7 \times 10^4 \pm 220$ cells/mm^2).

Discussion

In the current study, diffusion MRI was used to follow the response of a preclinical model of malignant lymphoma to a targeted nanotherapy (CRLX101) and its small molecule chemotherapy counterpart (CPT-11). As shown in Figs. 1 and 2, CRLX101 treatment led to quantifiable changes in ADC as early as day 2. By comparison, CPT-11 treatment also resulted in detectable changes in ADC, but was attenuated compared to the CRLX101 treatment. This attenuation is similar to what was observed by Lee et al (38), who demonstrated that attenuation or decrease of ADC values after an initial increase is indicative of tumor repopulation and emerging resistance. The ADC changes correlated with tumor growth kinetics, which indicated that CRLX101 treatment resulted in marked tumor regression while only mild regression was seen with CPT-11 treatment (Fig. 3). Moreover, the diffusion MRI results reflected histology. CRLX101 and CPT-11 treated tumors showed increased apoptotic events by day 2. Decreased cellularity was observed in both treatment cohorts compared to controls across the week. A decrease in the proliferation marker Ki-67 was also observed in both treatment cohorts. This reflects the fact that CPT inhibits cell proliferation and is concordant with previous studies showing high topoisomerase I inhibition by CRLX101 and CPT-11 within 48 hours of administration (6). Taken together, these results confirm the improved efficacy of CRLX101 compared to small molecule chemotherapy. Furthermore, diffusion MRI was able to demonstrate this improved efficacy at an early time point.

Other functional imaging techniques are being investigated to monitor early responses in lymphoma (16). Many of these studies involve nuclear imaging, specifically positron emission tomography (PET). In particular, ^{18}F-fluoro-2-deoxy-d-glucose (FDG-PET) (39) and 3'-^{18}F-fluoro-3'-deoxy-L-thymidine (40) are promising imaging biomarkers of lymphoma response. Interpretation of nuclear imaging studies can be complex, as many different physiological processes can result in a positive signal during treatment. For

example, local inflammation following therapy can increase the FDG-PET signal, masking treatment response (41). Diffusion MRI readouts are less sensitive to such inflammatory effects (42). Concerns of ionizing radiation over-exposure, especially in lymphoma patients who may be exposed to serial imaging scans and/or radiation therapy (43) also necessarily limits the number of nuclear imaging scans that can be obtained from a patient, especially at early treatment time points.

Although ADC by itself is already a promising imaging biomarker to indicate tumor response to CRLX101, the availability of ADC datasets from multiple time points enables mathematical modeling of tumor growth. This potentially allows the prediction of future treatment response in an individual patient. We applied a simple logistic model of tumor growth (26) to ADC data. The model makes the simplifying assumption that each imaging voxel consist only of tumor cells and that ADC changes are entirely due to the reduction in cellularity; yet it still provides instructive predictions using diffusion MRI datasets. This was shown by the strong correlation between simulated and estimated tumor cell number at both day 4 and day 7 (Fig. 4). Proliferation rates generated from this model separated CRLX101-treated and control groups (Fig. 5) and highlighted the enhanced anti-proliferative effect of CRLX101 (6). Analysis of proliferative rates across time points may add insights to a treatment's mode of action. For example, consideration of the CPT-11 ADC and tumor growth data alone through day 7 would indicate that the tumor may still be responding to treatment, albeit less than with the nanotherapy. However, analysis of the proliferation data indicated that between day 4 and 7 CPT-11 tumors showed a trend toward positive proliferation rates, suggesting treatment failure. The latter analysis is consistent with histology; by day 7 Ki-67 and apoptotic staining in CPT-11 tumors were similar to baseline and control. In contrast, CRLX101 proliferation rates were negative between day 0 and day 2, increased slightly between days 2 and 4 before decreasing again from day 4 to 7. This observation is consistent with CRLX101 Ki-67 staining, but is not immediately apparent from looking at ADC changes alone. The reason for this fluctuation of proliferation rate is unclear; tumor uptake and biochemical activity of CRLX101 have only been followed for up to 48 hours (6). Histological results showed that CC3 activity for CRLX101-treated tumors increased between day 0 and 2, decreased between days 2 and 4 before increasing again by day 7 (Supplementary Fig. 2). CRLX101-treated tumors also showed elevated TUNEL activity throughout the week compared to both CPT-11 and control. These results suggest that increased apoptosis contributes to the negative proliferation rates calculated from diffusion MRI data. The enhanced anti-tumor effect of CRLX101 may act via anti-angiogenesis and the nanotherapy's ability to prolong drug release via hydrolytic and enzymatic cleavage of the cyclodextrin-polymer (11). These factors may be synergistic, leading to the increased efficacy observed at the latter time point. Techniques that can probe CRLX101's dynamic anti-angiogenic effects within the tumor, such as dynamic contrast-enhanced MRI (44), may be able to elucidate this process.

Since it was difficult to spatially co-register individual tumor images across time points, imaging data were only analyzed at a whole-tumor ROI level. Thus, the heterogeneity of the tumor mass, which may also be an important determinant to treatment response, was not investigated. This may be addressed in future studies by prudent spatial co-registration across time points. Furthermore, the current model can be integrated into more sophisticated models (45) of tumor growth. Such models can account for the multiscale factors linking molecular scale phenomena to morphological tumor changes, including the multiple factors that can contribute to ADC changes during treatment response (42, 46–48), as well as by incorporating data acquired concurrently with other modalities (*e.g.* PET) (49, 50).

In conclusion, we have demonstrated that diffusion MRI can monitor the early response to CRLX101 treatment in a preclinical model of malignant lymphoma. Modeling of the ADC

data emphasized the enhanced anti-proliferative effect of CRLX101 compared to controls and CPT-11. This demonstrates the utility of diffusion MRI for preclinical and clinical evaluation of targeted nanotherapies such as CRLX101 and suggests that an image-driven modeling approach can provide insights to their mechanism(s) of action *in vivo*.

Supplementary Material

Refer to Web version on PubMed Central for supplementary material.

Acknowledgments

We thank Dr. Thomas Schluep of Calando Pharmaceuticals for providing the CRLX101, Dr. Andrey Demyanenko, Desiree Crow, Bita Alaghebandan, and Sonia Collazo for their technical assistance. Drs. Mark Davis, Yun Yen and Scott Fraser gave helpful advice and support.

Financial Support

The project was funded by NIBIB R01 EB000993, NIH R01 EB00194, NRSA T32GM07616, City of Hope Lymphoma SPORE Grant (P50 CA107399), the Beckman Institute and the Caltech/City of Hope Biomedical Initiative.

References

1. Davis ME, Chen ZG, Shin DM. Nanoparticle therapeutics: an emerging treatment modality for cancer. Nature reviews Drug discovery. 2008; 7:771–882.
2. Blanco E, Hsiao A, Mann AP, Landry MG, Meric-Bernstam F, Ferrari M. Nanomedicine in cancer therapy: innovative trends and prospects. Cancer science. 2011; 102:1247–1252. [PubMed: 21447010]
3. Cho K, Wang X, Nie S, Chen Z, Shin DM. Therapeutic Nanoparticles for Drug Delivery in Cancer. Clin Cancer Res. 2008; 14:1310–1316. [PubMed: 18316549]
4. Choi CH, Alabi CA, Webster P, Davis ME. Mechanism of active targeting in solid tumors with transferrin-containing gold nanoparticles. Proc Natl Acad Sci U S A. 2010; 107:1235–1240. [PubMed: 20080552]
5. Gribben JG. How I treat indolent lymphoma. Blood. 2007; 109:4617–4626. [PubMed: 17311989]
6. Numbenjapon T, Wang J, Colcher D, Schluep T, Davis ME, Duringer J, et al. Preclinical Results of Camptothecin-Polymer Conjugate (IT-101) in Multiple Human Lymphoma Xenograft Models. Clin Cancer Res. 2009; 15:4365–4373. [PubMed: 19549776]
7. Kuruvilla J. Standard therapy of advanced Hodgkin lymphoma. Hematology. 2009; 2009:497–506. [PubMed: 20008235]
8. Armitage JO. Early-Stage Hodgkin's Lymphoma. N Engl J Med. 2010; 363:653–662. [PubMed: 20818856]
9. Wall ME, Wani MC, Cook CE, Palmer KH, McPhail AT, Sim GA. Plant Antitumor Agents. I. The Isolation and Structure of Camptothecin, a Novel Alkaloidal Leukemia and Tumor Inhibitor from Camptotheca acuminata1,2. J Am Chem Soc. 1966; 88:3888–3890.
10. Davis ME. Design and development of IT-101, a cyclodextrin-containing polymer conjugate of camptothecin. Adv Drug Deliv Rev. 2009; 61:1189–1192. [PubMed: 19682514]
11. Schluep T, Hwang J, Hildebrandt IJ, Czernin J, Choi CH, Alabi CA, et al. Pharmacokinetics and tumor dynamics of the nanoparticle IT-101 from PET imaging and tumor histological measurements. Proc Natl Acad Sci U S A. 2009; 106:11394–11399. [PubMed: 19564622]
12. Schluep T, Hwang J, Cheng J, Heidel JD, Bartlett DW, Hollister B, et al. Preclinical Efficacy of the Camptothecin-Polymer Conjugate IT-101 in Multiple Cancer Models. Clin Cancer Res. 2006; 12:1606–1614. [PubMed: 16533788]
13. Yen Y, Coerver LA, Garmey EG, Kalinoski DL, Koczywas M, Neidhart JA, et al. Final phase 1/2a results evaluating the cyclodextrin-containing nanoparticle CRLX101 in patients with advanced solid tumor malignancies. Molecular Cancer Therapeutics. 2011; 10(Supplement 1)

14. Zhao B, Schwartz LH, Larson SM. Imaging Surrogates of Tumor Response to Therapy: Anatomic and Functional Biomarkers. J Nucl Med. 2009; 50:239–249. [PubMed: 19164218]
15. Eisenhauer EA, Therasse P, Bogaerts J, Schwartz LH, Sargent D, Ford R, et al. New response evaluation criteria in solid tumours: Revised RECIST guideline (version 1.1). Eur J Cancer. 2009; 45:228–247. [PubMed: 19097774]
16. Marcus CD, Ladam-Marcus V, Cucu C, Bouché O, Lucas L, Hoeffel C. Imaging techniques to evaluate the response to treatment in oncology: current standards and perspectives. Crit Rev Oncol Hematol. 2009; 72:217–238. [PubMed: 18760935]
17. Patterson DM, Padhani AR, Collins DJ. Technology Insight: water diffusion MRI[mdash]a potential new biomarker of response to cancer therapy. Nat Clin Prac Oncol. 2008; 5:220–233.
18. Huang MQ, Pickup S, Nelson DS, Qiao H, Xu HN, Li LZ, et al. Monitoring response to chemotherapy of non-Hodgkin's lymphoma xenografts by T2-weighted and diffusion-weighted MRI. NMR Biomed. 2008; 21:1021–1029. [PubMed: 18988250]
19. Lee KC, Moffat BA, Schott AF, Layman R, Ellingworth S, Juliar R, et al. Prospective Early Response Imaging Biomarker for Neoadjuvant Breast Cancer Chemotherapy. Clin Cancer Res. 2007; 13:443–450. [PubMed: 17255264]
20. Kim S, Loevner L, Quon H, Sherman E, Weinstein G, Kilger A, et al. Diffusion-Weighted Magnetic Resonance Imaging for Predicting and Detecting Early Response to Chemoradiation Therapy of Squamous Cell Carcinomas of the Head and Neck. Clin Cancer Res. 2009; 15:986–994. [PubMed: 19188170]
21. Hamstra DA, Galbán CJ, Meyer CR, Johnson TD, Sundgren PC, Tsien C, et al. Functional Diffusion Map As an Early Imaging Biomarker for High-Grade Glioma: Correlation With Conventional Radiologic Response and Overall Survival. J Clin Oncol. 2008; 26:3387–3394. [PubMed: 18541899]
22. Hamstra DA, Chenevert TL, Moffat BA, Johnson TD, Meyer CR, Mukherji SK, et al. Evaluation of the functional diffusion map as an early biomarker of time-to-progression and overall survival in high-grade glioma. Proc Natl Acad Sci U S A. 2005; 102:16759–16764. [PubMed: 16267128]
23. Lazovic J, Jensen MC, Ferkassian E, Aguilar B, Raubitschek A, Jacobs RE. Imaging Immune Response In vivo: Cytolytic Action of Genetically Altered T Cells Directed to Glioblastoma Multiforme. Clin Cancer Res. 2008; 14:3832–3839. [PubMed: 18559603]
24. Reddy GR, Bhojani MS, McConville P, Moody J, Moffat BA, Hall DE, et al. Vascular Targeted Nanoparticles for Imaging and Treatment of Brain Tumors. Clin Cancer Res. 2006; 12:6677–6686. [PubMed: 17121886]
25. Deisboeck TS, Wang Z, Macklin P, Cristini V. Multiscale cancer modeling. Annu Rev Biomed Eng. 2011; 13:127–155. [PubMed: 21529163]
26. Yankeelov TE, Atuegwu NC, Deane NG, Gore JC. Modeling tumor growth and treatment response based on quantitative imaging data. Integr Biol (Camb). 2010; 2:338–345. [PubMed: 20596581]
27. Atuegwu NC, Colvin DC, Loveless ME, Xu L, Gore JC, Yankeelov TE. Incorporation of diffusion-weighted magnetic resonance imaging data into a simple mathematical model of tumor growth. Phys Med Biol. 2012; 57:225. [PubMed: 22156038]
28. Ellingson BM, LaViolette PS, Rand SD, Malkin MG, Connelly JM, Mueller WM, et al. Spatially quantifying microscopic tumor invasion and proliferation using a voxel-wise solution to a glioma growth model and serial diffusion MRI. Magn Reson Med. 2011; 65:1131–1143. [PubMed: 21413079]
29. Xinjian C, Summers R, Jianhua Y. FEM-Based 3-D Tumor Growth Prediction for Kidney Tumor. Biomedical Engineering, IEEE Transactions on. 2011; 58:463–467.
30. Swanson KR, Rockne RC, Claridge J, Chaplain MA, Alvord EC, Anderson AR. Quantifying the role of angiogenesis in malignant progression of gliomas: In silico modeling integrates imaging and histology. Cancer Res. 2011
31. Thurber GM, Weissleder R. A systems approach for tumor pharmacokinetics. PloS one. 2011; 6:e24696. [PubMed: 21935441]
32. Brown CE, Wright CL, Naranjo A, Vishwanath RP, Chang W-C, Olivares S, et al. Biophotonic cytotoxicity assay for high-throughput screening of cytolytic killing. J Immunol Methods. 2005; 297:39–52. [PubMed: 15777929]

33. Lebihan D, Breton E. Imagerie de Diffusion In Vivo par Résonance Magnétique Nucléaire. XXX CR Académie des Sciences de Paris. 1985; 301:1109–1112.
34. Stejskal EO, Tanner JE. Spin Diffusion Measurements: Spin Echoes in the Presence of a Time-Dependent Field Gradient. J Chem Phys. 1965; 42:288–292.
35. Thomas DL, Lythgoe MF, Pell GS, Calamante F, Ordidge RJ. The measurement of diffusion and perfusion in biological systems using magnetic resonance imaging. Phys Med Biol. 2000; 45:R97–R138. [PubMed: 10958179]
36. Tuominen VJ, Ruotoistenmaki S, Viitanen A, Jumppanen M, Isola J. ImmunoRatio: a publicly available web application for quantitative image analysis of estrogen receptor (ER), progesterone receptor (PR), and Ki-67. Breast cancer research : BCR. 2010; 12:R56. [PubMed: 20663194]
37. Ruifrok AC, Johnston DA. Quantification of histochemical staining by color deconvolution. Anal Quant Cytol Histol. 2001; 23:291–299. [PubMed: 11531144]
38. Lee KC, Hall DE, Hoff BA, Moffat BA, Sharma S, Chenevert TL, et al. Dynamic Imaging of Emerging Resistance during Cancer Therapy. Cancer Res. 2006; 66:4687–4692. [PubMed: 16651420]
39. Ben-Haim S, Ell P. 18F-FDG PET and PET/CT in the Evaluation of Cancer Treatment Response. J Nucl Med. 2009; 50:88–99. [PubMed: 19139187]
40. Graf N, Herrmann K, den Hollander J, Fend F, Schuster T, Wester H-J, et al. Imaging Proliferation to Monitor Early Response of Lymphoma to Cytotoxic Treatment. Molecular Imaging and Biology. 2008; 10:349–355. [PubMed: 18704591]
41. van Waarde A, Cobben DCP, Suurmeijer AJH, Maas B, Vaalburg W, de Vries EFJ, et al. Selectivity of 18F-FLT and 18F-FDG for Differentiating Tumor from Inflammation in a Rodent Model. Journal of Nuclear Medicine. 2004; 45:695–700. [PubMed: 15073267]
42. Galbán CJ, Bhojani MS, Lee KC, Meyer CR, Van Dort ME, Kuszpit KK, et al. Evaluation of Treatment-Associated Inflammatory Response on Diffusion-Weighted Magnetic Resonance Imaging and 2-[18F]-Fluoro-2-Deoxy-d-Glucose-Positron Emission Tomography Imaging Biomarkers. Clin Cancer Res. 2010; 16:1542–1552. [PubMed: 20160061]
43. Fazel R, Krumholz HM, Wang Y, Ross JS, Chen J, Ting HH, et al. Exposure to Low-Dose Ionizing Radiation from Medical Imaging Procedures. N Engl J Med. 2009; 361:849–857. [PubMed: 19710483]
44. Padhani AR. Dynamic contrast-enhanced MRI in clinical oncology: Current status and future directions. J Magn Reson Imaging. 2002; 16:407–422. [PubMed: 12353256]
45. Atuegwu NC, Gore JC, Yankeelov TE. The integration of quantitative multi-modality imaging data into mathematical models of tumors. Phys Med Biol. 2010; 55:2429–2449. [PubMed: 20371913]
46. Lyng H, Haraldseth O, Rofstad EK. Measurement of cell density and necrotic fraction in human melanoma xenografts by diffusion weighted magnetic resonance imaging. Magn Reson Med. 2000; 43:828–836. [PubMed: 10861877]
47. Xu J, Li K, Smith RA, Waterton JC, Zhao P, Chen H, et al. Characterizing Tumor Response to Chemotherapy at Various Length Scales Using Temporal Diffusion Spectroscopy. PloS one. 2012; 7:e41714. [PubMed: 22911846]
48. Thoeny HC, Ross BD. Predicting and monitoring cancer treatment response with diffusion-weighted MRI. J Magn Reson Imaging. 2010; 32:2–16. [PubMed: 20575076]
49. Ng TSC, Procissi D, Wu Y, Jacobs RE. A robust coregistration method for in vivo studies using a first generation simultaneous PET/MR scanner. Med Phys. 2010; 37:1995–2003. [PubMed: 20527533]
50. Ng TSC, Bading JR, Park R, Sohi H, Procissi D, Colcher D, et al. Quantitative, Simultaneous PET/MRI for Intratumoral Imaging with an MRI-Compatible PET Scanner. Journal of Nuclear Medicine. 2012; 53:1102–1109. [PubMed: 22661534]

Translational Relevance

Targeted nanotherapies are being developed for cancer treatment. The advantage of these therapies over conventional treatments lies in their ability to increase drug uptake in tumors while reducing treatment-related toxicity. Clinically-applicable biomarkers will facilitate translation of nanotherapies to the clinic. We evaluated the applicability of diffusion MRI to monitor CRLX101 (a cyclodextrin-based polymer particle containing the DNA topoisomerase I inhibitor camptothecin) efficacy in a preclinical model of malignant lymphoma. Diffusion MRI distinguished animals treated with CRLX101 from controls as early as day 2 post-treatment. Diffusion MRI also demonstrated the reduced efficacy of irinotecan compared to CRLX101. Incorporating diffusion MRI data into a mathematical model of tumor growth allowed prediction of the enhanced anti-proliferative effect of CRLX101 as compared to irinotecan. These results demonstrate that serial imaging using diffusion MRI, combined with judicious modeling of imaging data, provides useful biomarkers to evaluate, monitor and predict the efficacy of targeted nanotherapies in the clinic.

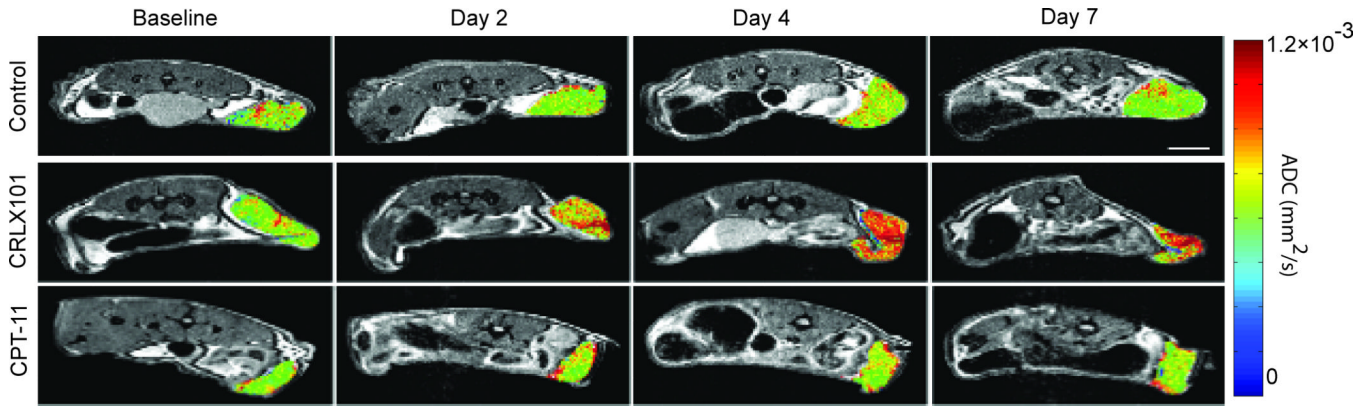

Figure 1.

Diffusion MRI is sensitive to early CRLX101 response. Representative ADC maps of Daudi tumors are shown as color overlays on T2-weighted anatomic MRI images. Diffusion MRI images were acquired on day 0 (pre-treatment), day 2, day 4 and day 7 for control (top row), CRLX101 treated (middle row) and CPT-11 treated (bottom row). Diffusion MRI clearly shows an increased ADC response to CRLX101 throughout the whole tumor mass as early as day 2 post treatment, compared to CPT-11 treated and control animals (Scale bar = 10 mm).

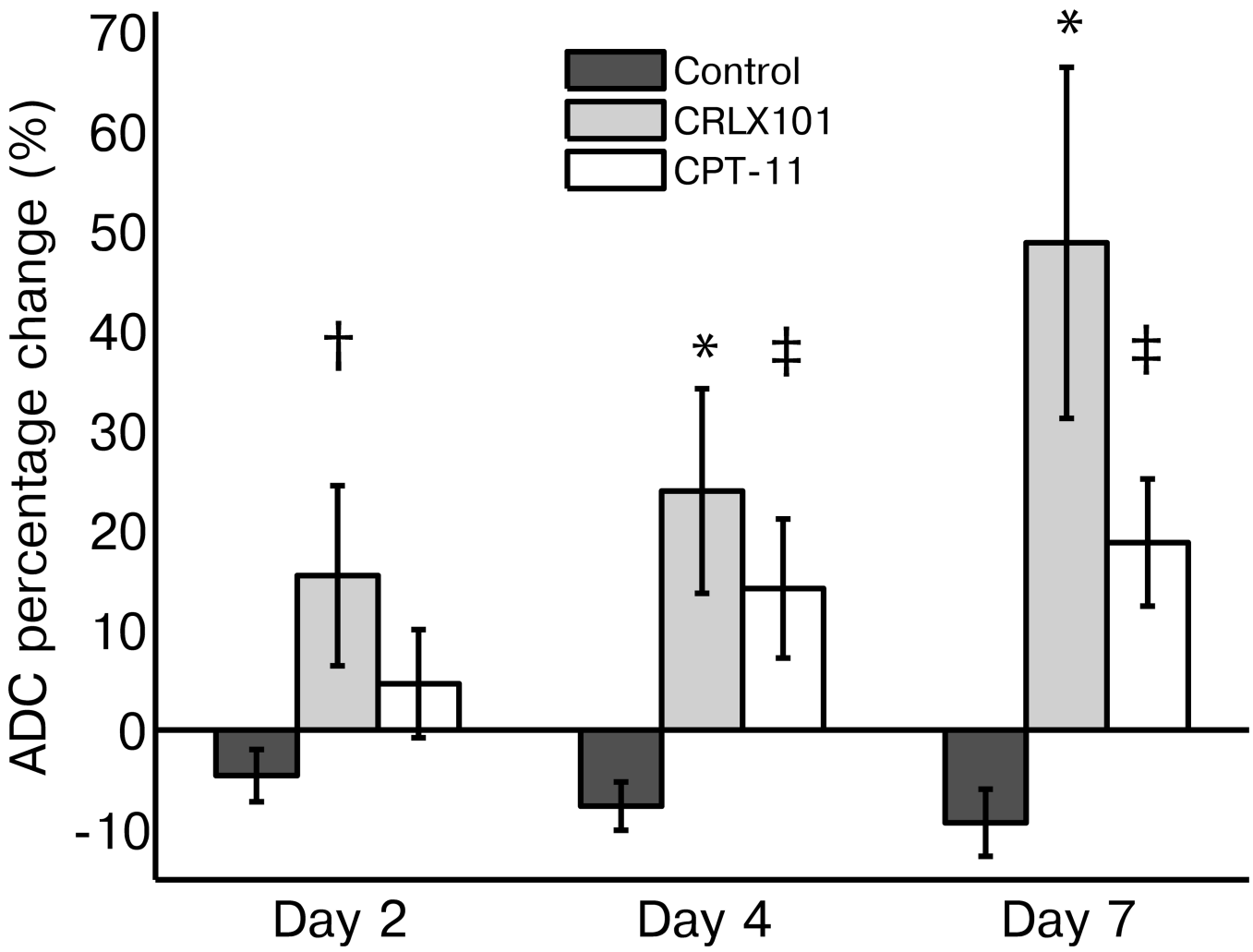

Figure 2.

ADC changes over treatment week show efficacy of CRLX101. Percentage change of mean ADC values compared to baseline is graphed for the three different treatment groups over one week post treatment. CPT-11 animals showed a slight increase in the ADC values over the week compared to baseline, while control animals showed a slight decrease. CRLX101 treated animals showed an increase in ADC values at all time points. Compared to the control cohort, ADC increases observed in CRLX101-treated animals were significant on all days (day 2: $p = 0.02$, †, day4: $p < 0.01$, *, day 7: $p < 0.01$, *). This was not the case for the CPT-11 group (day 2: $p = 0.4$, day4: $p = 0.05$, ‡, day 7: $p = 0.05$, ‡). Error bars denote standard error.

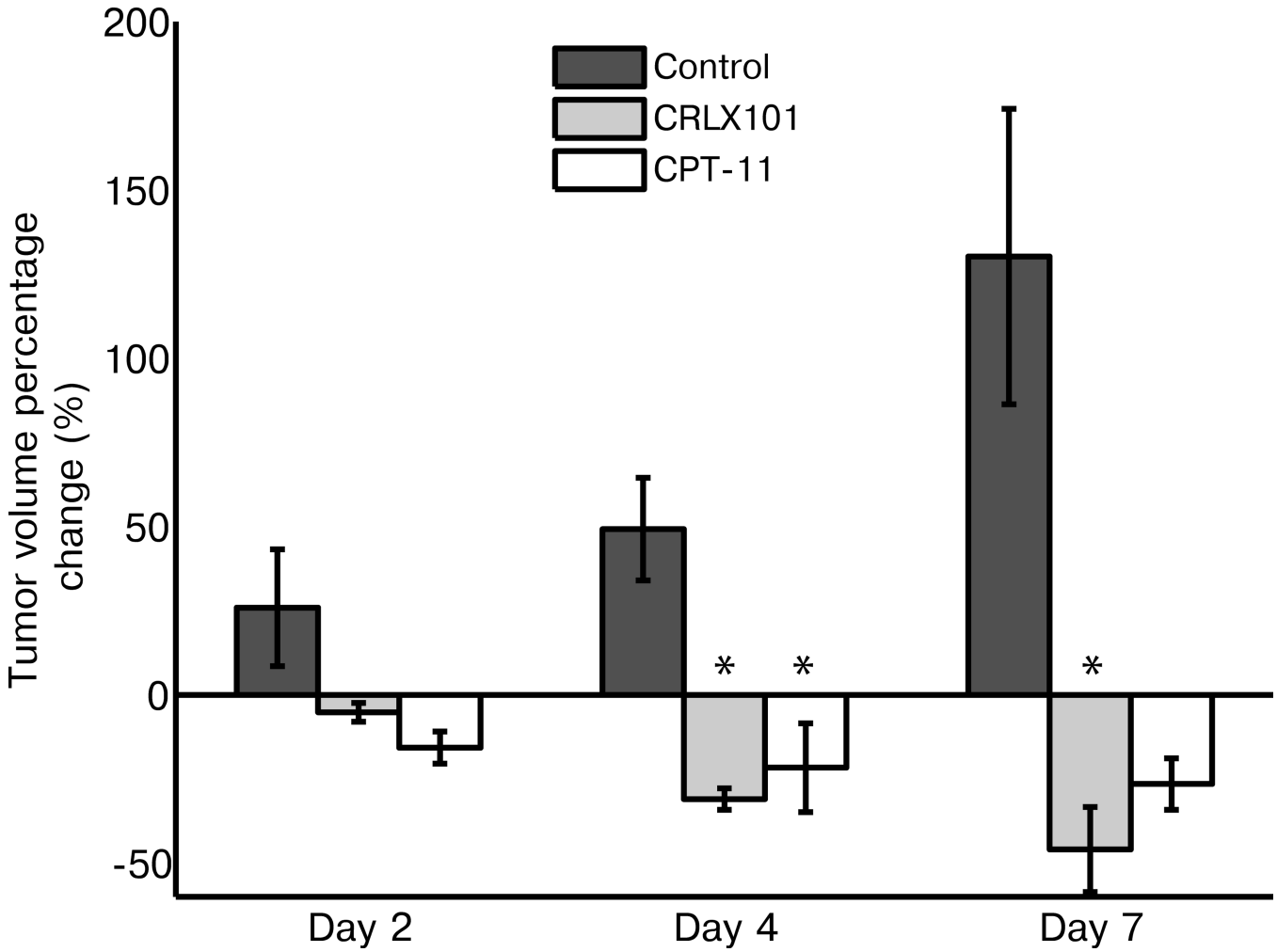

Figure 3.
Tumor volume size changes over treatment week. Mean tumor sizes, as measured from anatomical MRI images, are graphed for the three different treatment groups over one week post treatment. Compared to controls, CRLX101 tumor sizes significantly decreased on both day 4 and 7 ($p < 0.01$, *). In comparison, CPT-11 group tumor size changes were only significantly different to the control group on day 4 ($p < 0.01$, *). Error bars denote standard error.

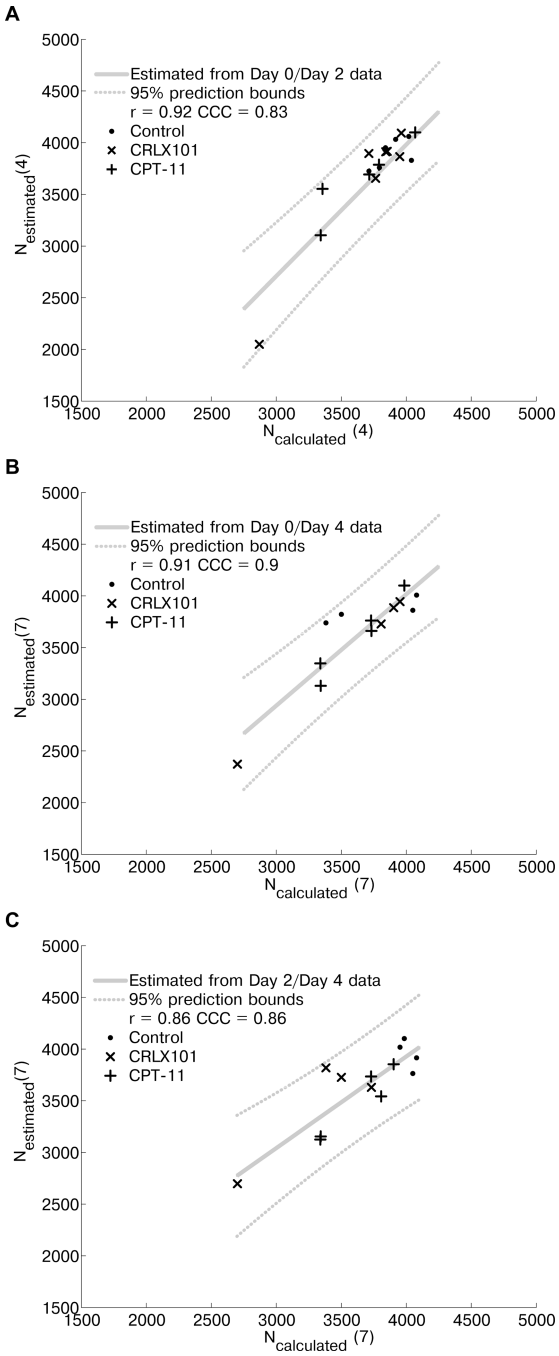

Figure 4.

A logistic model of tumor growth can be applied to ADC data. (A) $N_{calculated}(4)$ (using ADC data from day 0 and day 2) is compared to $N_{estimated}(4)$. The linear fit (with 95% prediction intervals) is also plotted. The Pearson's correlation coefficient, r, is 0.92 ($p < 0.0001$) and the concordance correlation coefficient, CCC, is 0.83. (B) $N_{calculated}(7)$ (using ADC data from day 0 and day 4) is compared to $N_{estimated}(7)$. r = 0.91 ($p < 0.0001$) and CCC = 0.9. (C) $N_{calculated}(7)$ (using ADC data from day 2 and day 4) is compared to $N_{estimated}(7)$. r = 0.86 ($p < 0.0001$) and CCC = 0.86.

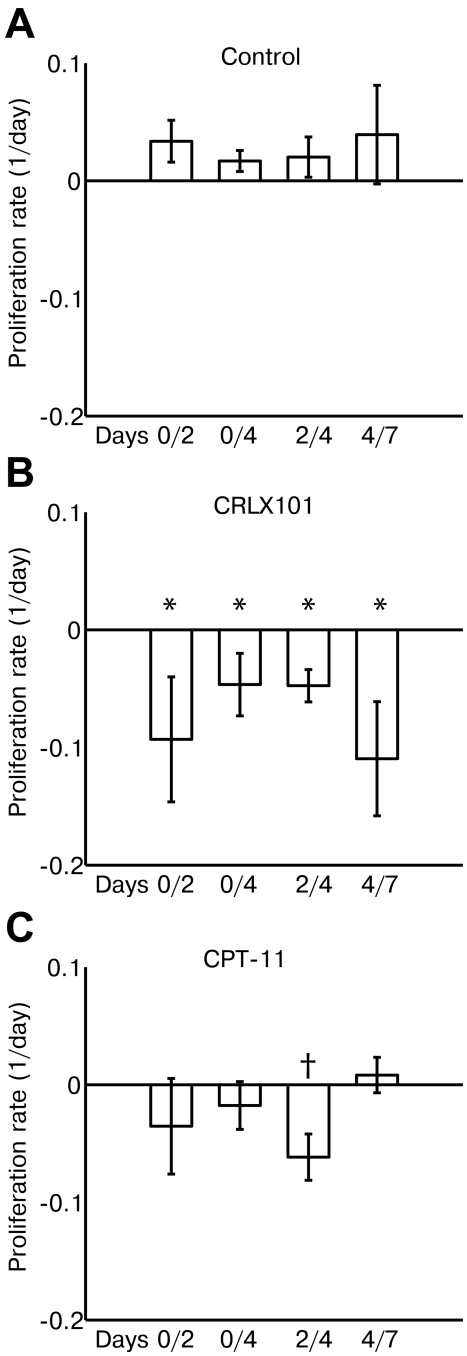

Figure 5.

Cellular proliferation rates for different treatment groups were calculated by applying ADC data to a logistic model of tumor growth. Rates were calculated for (A) control, (B) CRLX101 and (C) CPT-11 animals between day 0/2, day 0/4, day 2/4, and day 4/7. Rates from CRLX101 animals were negative for all time periods and were significantly different to controls ($p = 0.02$, *). Rates for CPT-11 animals were negative between day 0 to day 4, being significantly different to controls between day 2/4 ($p = 0.03$, †). By day 4/7, CPT-11 proliferation rates became positive and similar to controls. Error bars denote standard error.

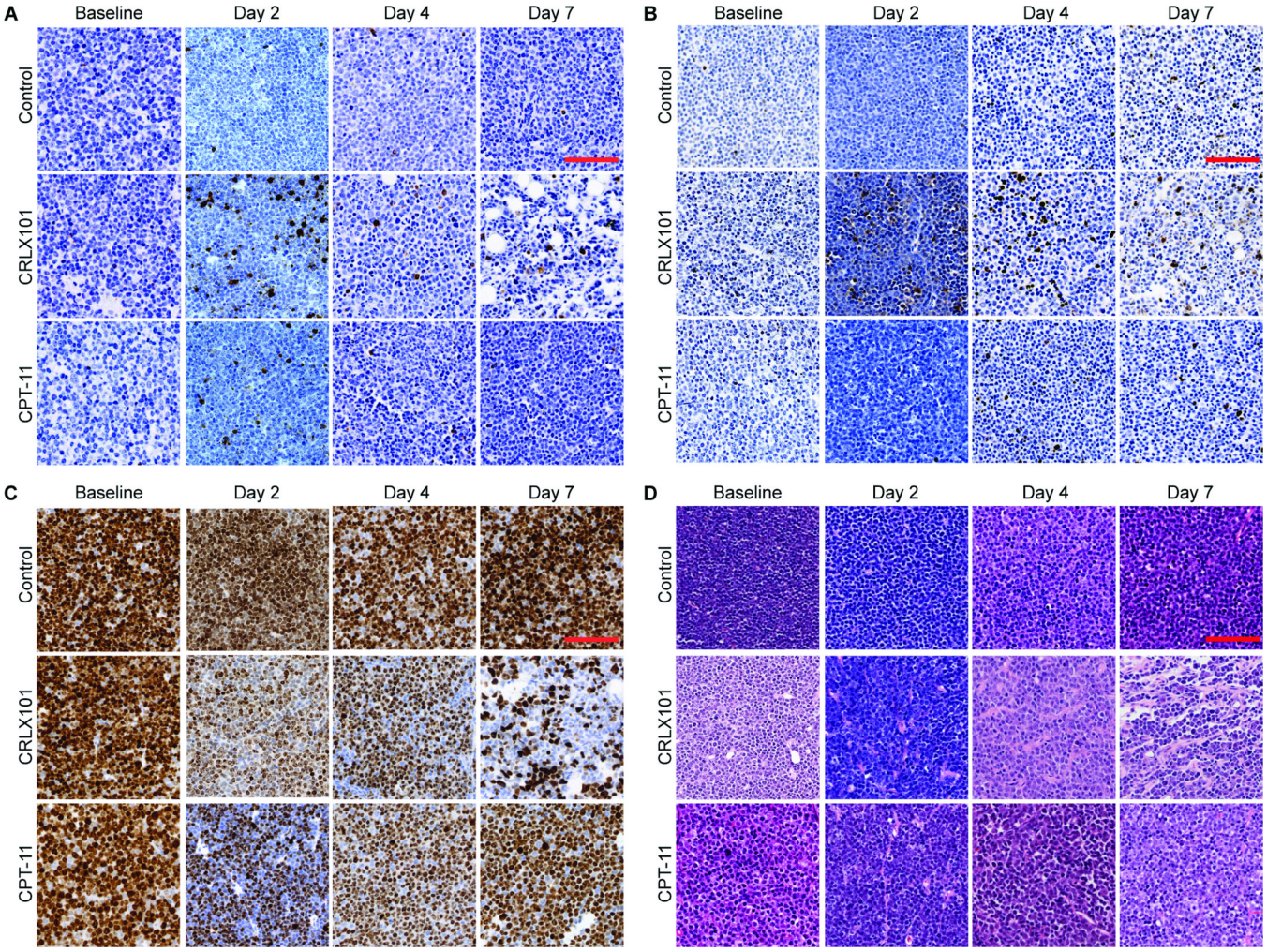

Figure 6.

Histological assessment of CRLX101 and CPT-11 response. Tumors treated with CRLX101 (5 mg/kg), CPT-11 (100 mg/kg) or saline were harvested for histology on days 0, 2, 4, and 7. Tumor samples were subsequently sectioned and stained with (A) Cleaved caspase-3 (CC3, co-stained with hematoxylin), (B) TUNEL (co-stained with hematoxylin), (C) Ki-67 (co-stained with hematoxylin) and (D) H&E. Compared to controls both CRLX101 and CPT-11 showed increased CC3 activity and decreased Ki-67 activity by day 2 post-treatment, shown by the increased staining. This reflects the anti-proliferative, anti-tumor activity of both agents. CRLX101 treated tumors showed an increased magnitude of these effects, highlighting its improved efficacy compared to CPT-11. Supplementary Figure 2 and Supplementary Table 1 provide further analysis of the histology (scale bar = 500 μm).